*Journal of Electron Microscopy*: 1–8 (2010)
doi: 10.1093/jmicro/dfq056

Biological: Full-length

# Comparison of the envelope architecture of *E. coli* using two methods: CEMOVIS and cryo-electron tomography

Aiko Kishimoto-Okada[1,2], Satoshi Murakami[3], Yoshiko Ito[4], Noritaka Horii[5], Hiromitsu Furukawa[5], Junichi Takagi[1] and Kenji Iwasaki[1,2,*]

[1]Institute for Protein Research, Laboratory of Protein Synthesis and Expression, Osaka University, 3-2 Yamadaoka, Suita, Osaka 565-0871, Japan, [2]Core Research for Evolution Science and Technology (CREST), Japan Science and Technology Agency, 3-2 Yamadaoka, Suita, Osaka 565-0871, Japan, [3]School and Graduate School of Bioscience and Biotechnology, Tokyo Institute of Technology, 4259 Nagatsuta-cho, Midori-ku, Yokohama, Kanagawa 226-8503, Japan, [4]Leica Microsystems K.K., 1-27-6 Shirokane, Minato-ku, Tokyo 108-0072, Japan [5]JEOL System Technology Co., Ltd, 3-1-2 Musashino, Akishima, Tokyo 196-8558, Japan
*To whom correspondence should be addressed. E-mail: ikenji@protein.osaka-u.ac.jp

**Abstract** Cryo-electron microscopy of vitreous sections (CEMOVIS) and cryo-electron tomography (cryo-ET) of vitrified specimens are gradually gaining popularity. However, similar to the conventional methods, these techniques tend to produce different images of the same sample. In CEMOVIS, the mechanical stress caused by sectioning may cause inaccuracies smaller than those caused by crevasses. Therefore, we examined *Escherichia coli* cells by using CEMOVIS and cryo-ET to determine the differences in the computed sizes of the envelope layers, which are smaller than crevasses. We found that the width of the periplasmic space in vitreous sections and tomograms was 12 and 14 nm, respectively; furthermore, while the distance between the outer membrane (OM) and the peptidoglycan (PG) layer was almost equal (11 nm) in the two techniques, that between the plasma membrane (PM) and PG was clearly different. Thus, the observed size difference can be mainly attributed to the PM–PG distance. Since our data were obtained from images acquired using the same microscope in the same conditions, the size differences cannot be attributed to microscope-related factors. One possible factor is the angle of the cutting plane against the long axis of the cell body in CEMOVIS. However, the same PG–OM distance in both methods may exclude the variations caused by this factor. Furthermore, the mechanical stress caused by vitreous sectioning or high-pressure freezing may result in shrinkage. If this shrinkage is responsible for the nanometre-scale deformation in CEMOVIS, this factor will have to be considered in determining the molecular resolution obtained by CEMOVIS.

**Keywords** cryosection, CEMOVIS, cryo-electron tomography, vitreous ice, *E. coli*

**Received** 18 March 2010, accepted 2 June 2010

## Introduction

Advances in the methodological developments of cryo-electron microscopy (cryo-EM) of vitrified biological molecules show the possibility of molecular imaging at near-atomic resolution, as long as an object has high symmetry [1]. However, this technique is limited largely to the observation of isolated proteins or their complexes because the thickness of vitreous ice must be maintained at the submicrometre level. Application of the vitrification technique to larger biological samples such as tissues, which has been pioneered mainly by Dubochet and

co-workers, should fulfil the great demand to observe various biological specimens as close to the native state as possible [2]. Indeed, even at the expense of the low-contrast image, this technique has considerable advantages, including the avoidance of molecule denaturation by dehydration and chemical linking and the prevention of loss of unlinked molecules due to the dewatering. In spite of these advantages, however, new techniques always need to be rigorously evaluated to clarify the question 'What purpose is this technique appropriate for?' Dubochet's group and other groups have already published various reports related to cryo-electron microscopy of vitreous sections (CEMOVIS) in which certain artefacts, such as knife marks, compression, crevasses and chatter, are mentioned [3–5]. Since these artefacts occur at a very large scale, they are unlikely to influence microstructures, including molecular structures. In order to gain an estimate of the extent to which the vitreous sectioning process affects microstructures smaller than 0.1 μm in size, we examined *Escherichia coli* K-12 using both cryo-electron tomography (cryo-ET) and CEMOVIS and cross-validated their images. Amorphous frozen-hydrated sections of *E. coli* were originally reported by Dubochet *et al.* in 1983 [6] and refinements of the technique were reported in 2003 [7]. As these authors focused mainly on the cell envelope in their observation, we also paid particular attention to the envelope architecture composed of three layers – outer membrane (OM), peptidoglycan (PG) layer and plasma membrane (PM) – to evaluate the differences in their size as determined by cryo-ET and CEMOVIS. The same type of analysis was reported by Hoffmann *et al.* [8] who used *E. coli* DH5α as a control to study the mycobacterial OM using cryo-ET and CEMOVIS. We attempted systematic comparison of the same specimen (*E. coli*) by using two methods, CEMOVIS and cryo-EM; the assessments were performed using the same microscope in identical conditions with a little ingenuity in the measurements of the envelope layers.

## Materials and methods

### Culture conditions

*E. coli* BL21(DE3) was grown in 2× YT medium at 37°C for 16 h.

### Vitreous sectioning

Suspension cultures of *E. coli* BL21 (DE) were concentrated by low-speed centrifugation at 15 000 rpm (21 900×*g*). The resultant pellet was suspended in an extracellular cryoprotectant (30% dextran, 100–200 kDa) and was centrifuged at the same speed for 20 min, resulting in the recovery of the cells in the supernatant fraction because of the high density of dextran. The supernatant was then drawn into copper capillary tubes specialized for the EMPACT-2 high-pressure freezing machine (Leica Microsystems, Wetzlar, Germany). Cryosections of *E. coli* in the vitreous phase were prepared using an Ultracut FC6 cryoultramicrotome (Leica Microsystems, Wetzlar, Germany) at a temperature of ~−160°C. Seventy-nanometre feed cryosections were cut using a 35° diamond knife (Diatome, Hatfield, PA) with a clearance angle of 6°. The cutting speed was 1.2 nm/s. The sections were transferred using a toothbrush to a copper grid covered with a continuous carbon film.

### Vitrification

A 5-μl droplet of resuspended *E. coli* pellet, obtained after centrifugation at 15 000 rpm (21 900×*g*), was placed on a C-flat grid (Protochips, Raleigh, NC) in the chamber of a Vitrobot (FEI, Hillsboro, OR) [9,10] at 80% humidity and 4°C. All the processes, blotting and plunge-freezing into liquid ethane were performed by the Vitrobot.

### Cryo-electron microscopy

Vitreous sections and vitrified non-sectioned samples were examined using a JEM-3200FSC/BU transmission electron microscope (JEOL, Tokyo, Japan) incorporating a liquid helium stage and an omega-type energy filter operating at 300 kV. A slit width of 20 eV was used to obtain a zero energy loss electron beam. The specimen was tilted about one axis in 1° increments over a total angular range of ±30°. Since there was no automated data acquisition software, each tilt series was performed manually. Each image was captured at 1.6 pA/cm$^2$ on a fluorescent screen, which is equal to 0.9 $e^-$/Å$^2$ as an electron dose for a 1-s exposure time. However, this value is underestimated because the beam current on the fluorescent screen was measured after electrons had

passed through the omega-type filter. The cryosections were recorded at 5.2 pA/cm$^2$, which corresponds to 2.9 $e^-$/Å$^2$. The recording device we used was a 4096 × 4096 pixel CCD camera (TVIPS, Gauting, Germany). The pixel size, calibrated using a crystal of catalase, was 0.31 nm at a nominal magnification of ×30 000.

### Image processing

#### Tomography

Initially, the images obtained from a tilt series were aligned using IMOD [11]. The pre-aligned images were then re-aligned and three-dimensional (3-D) images were reconstructed using the simultaneous iterative reconstruction technique [12] by TEMOGRAPHY (JEOL System, Tokyo, Japan).

### Measurement of various distances

Images were sectioned using EOS [13] and averaged density profiles across the cell envelope structures were calculated for each section. The distances between peaks were measured by fitting a Gaussian curve to the profiles. All of these measurement procedures were performed using Matlab (MathWorks, Natick, MA).

## Results

### Vitreous sectioning of *E. coli*

Preparation of vitreous ice sections was performed according to the established method described by Dubochet [2,14]. High-pressure freezing was performed in copper tubes to which the cell suspension was sucked. The cryo-EM images of a frozen-hydrated section of *E. coli* were quite similar to those reported previously, and the three major layers – OM, PG and PM – were readily discernible (Fig. 1). In Fig. 1, the knife marks running from the upper right to the lower left indicate the cutting direction. The ellipsoidal shape of the bacterial cells, which is due to deformation of the specimen caused by compression during cryosectioning, is consistent with the previous report [7]. The regions facing toward the cutting direction (i.e. the upper right and the lower left area in Fig. 1) showed the most severe deformation and thus are not suitable for the further analysis.

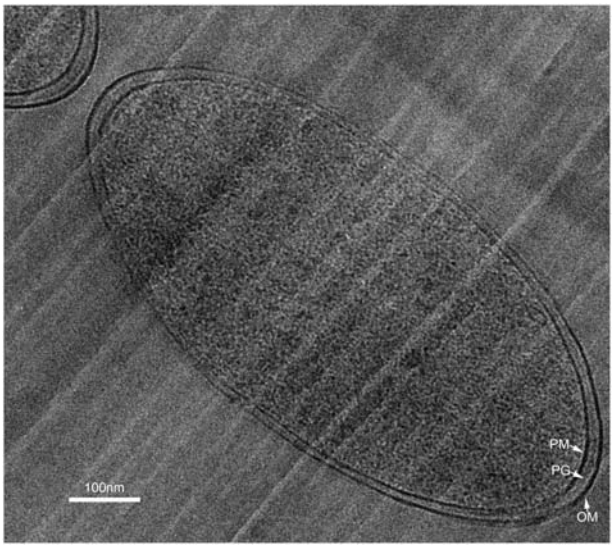


**Fig. 1.** An energy-filtered image of a cryosection of *E. coli* K-12. OM, PG and PM are indicated by arrows. White knife marks run from the top right to the bottom left (or reverse). Fortunately, there are no crevasses in this area. Bar, 100 nm.

### Cryo-ET of vitreous ice-embedded intact bacterial cells

Whole-mounted *E. coli* cells are too thick for cryo-EM to reveal details of the cytoplasm. However, in every case, the peripheral region of the *E. coli* cell clearly shows the outer and inner membranes (Fig. 2). Cryo-ET was performed manually at 4 K using a liquid helium stage. A field emission gun operated at 300 kV accelerated voltage produced strong brightness. However, the higher the angle at which the specimen is tilted, the thicker the specimen is along the beam direction, which creates a lower signal-to-noise ratio. We compared the tomogram reconstructed from a tilt series acquired using 2° steps, including the images of the specimen tilted at a high angle until ±60°, with that reconstructed from a tilt series ranging from –30 to +30° acquired using 1° steps. The latter procedure yielded clearer structures in the peripheral region, and we decided to use tomograms reconstructed from the low-tilt series for the following measurements. We particularly made full use of the local alignment technique to obtain better tomograms [15]. First, the coarse alignment was calculated and then the regions of interest were cut out from the coarse-aligned tilt series. These sub-tilt series were then re-aligned. The slices of the 3-D tomograms show the architecture of the cell wall of *E. coli* clearer than the snapshot (Fig. 2a).

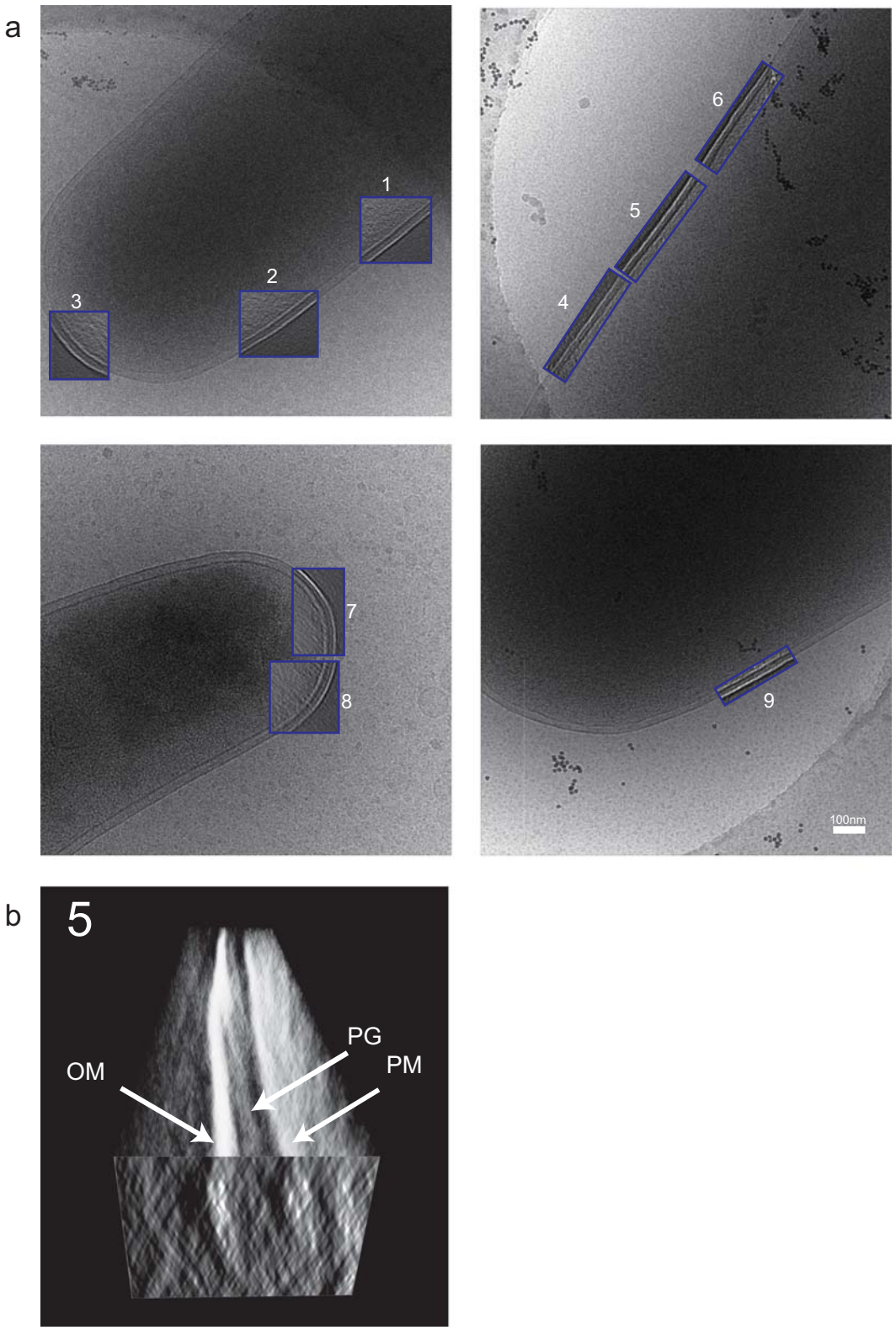


**Fig. 2.** (a) Vitreous ice-embedded intact *E. coli*. Tomographic reconstruction was performed using these four bacterial cells. The slices of the tomograms used for measurement of the envelope layer distances are superimposed on the location corresponding to that in the cryo-EM image. Each slice is numbered. Bar, 100 nm. (b) 3-D view of tomogram no. 5 in (a) with a vertical section (front side).

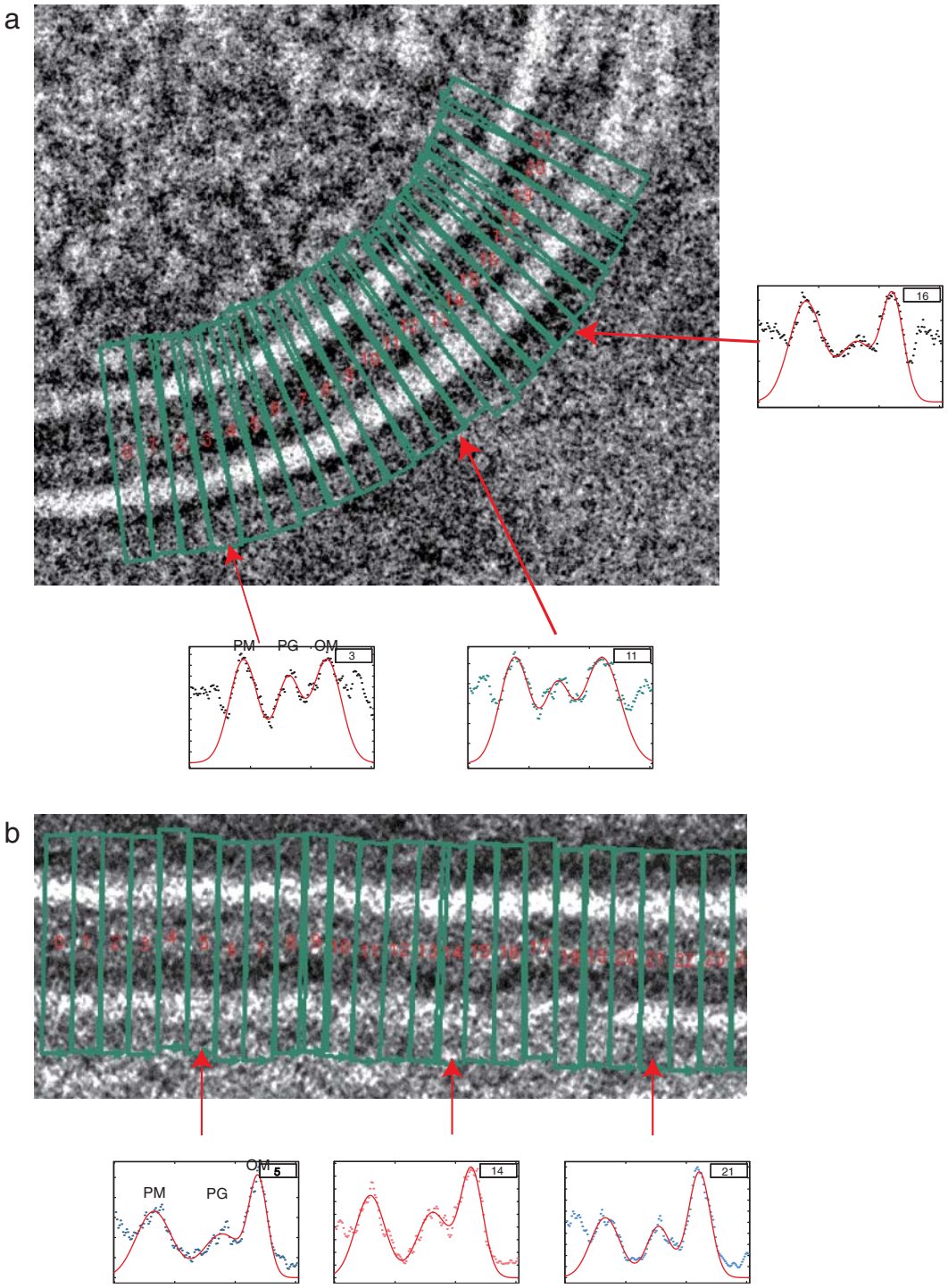


**Fig. 3.** Measurements of the three envelope layers using fragmentation in (a) CEMOVIS and in (b) tomogram. (a) The envelope region from central slice of the tomogram was extracted into rectangular boxes. In this case, 60 boxes were used for the extraction. The density profiles of some of the boxes (nos. 3, 11, and 16) are plotted. (b) After alignment of these boxed-out images by calculating cross-correlation, they were plotted. High-density peaks clearly show three layers: PM, PG and OM. The high density, which included the densities of the lipids and proteins, is represented as a positive value.

## Measurement of the envelope architecture

In order to evaluate the structural preservation in *E. coli* cells achieved by cryosectioning, we made measurements of the distances between the envelope layers in both cryosections and cryo-tomograms. Although values for these measurements have been reported by several researchers, the accurate measurements are difficult due to the noise, unclear

**Table 1.** Distance in the cell envelope of *Escherichia coli*

| | Peak to peak distance | | | | | |
|---|---|---|---|---|---|---|
| | Tomograms (nm) | | | | CEMOVIS (nm) | |
| Place of *E.Coli* | Lateral | | Pole | | Lateral | |
| Index \ Distance | PM-PG | PG-OM | PM-PG | PG-OM | PM-PG | PG-OM |
| 1 | 15.5 | 11.5 | | | 13.0 | 11.0 |
| 2 | 14.4 | 12.1 | | | 11.6 | 10.9 |
| 3 | | | 15.4 | 13.0 | 11.5 | 10.6 |
| 4 | 14.7 | 10.1 | | | 11.4 | 11.3 |
| 5 | 13.6 | 10.7 | | | 12.9 | 11.3 |
| 6 | 15.0 | 9.7 | | | 11.8 | 10.7 |
| 7 | | | 15.8 | 11.4 | | |
| 8 | | | 17.0 | 12.4 | | |
| 9 | 13.1 | 10.0 | | | | |
| Average | 14.4 | 10.7 | 16.1 | 12.3 | 12.0 | 11.0 |
| SD | ±0.9 | ±0.9 | ±0.8 | ±0.8 | ±0.7 | ±0.3 |
| t-test | | | 5.0 | 0.4 | | |

layer boundaries and undulating layers. Notably, the thickness of the layers changes dramatically depending on the grey-scale value selected. Moreover, the notorious noise in the cryo-images makes it difficult to identify the exact shape. Therefore, to overcome this problem, we used a little ingenuity. In the case of tomography, one of the slices was extracted from the centre of the tomogram for the measurements of the distances. The 3-D view and the vertical section of the tomogram in Fig. 2b show that the central section is appropriate for measuring the distances between the layers, irrespective of the large missing wedge caused by the small range of tilt angles (−30 to +30°). For cryosections, the images themselves were used for measurements. In either case, the envelope regions were boxed out into thin rectangular-shaped areas along the envelope, as depicted in Fig. 3a and b (green boxes). Mutually adjacent extracted images were then aligned. This segmentation reduces the measurement errors caused by non-linear layers. As a next step, the pixel density along the short axis of each rectangular box was averaged in order to reduce the noise. To increase the precision of the measurement, we attempted to fit three Gaussian curves to the plot, which enabled us to identify the peak positions of the PM, PG and OM (Fig. 3). Thus, the peak-to-peak distances could be measured, as summarized in

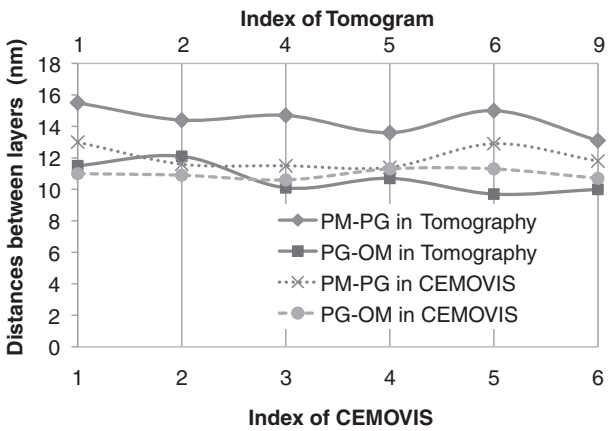


**Fig. 4.** Graph of distance data in the lateral region. The graph clearly shows that the PM–PG distances in tomograms are larger than the other distances.

Table 1 and Fig. 4. Another important point to mention is that, in the tomograms, we measured these structures at two different positions in the bacterial cell, namely, in a lateral region and in a pole region. In contrast, the measurement of distances in cryosectioned samples was limited to a single lateral position due to the severe deformation caused by the sectioning. As a consequence, the distance measured in the cryosections corresponds to that of the lateral position of the bacterial body in the tomograms. The parts corresponding to the index numbers listed in Table 1 are indicated in Fig. 2. The average values for the distances between PG and OM are very similar in the tomograms and cryosections. On the other hand, the distances between PM and PG in the tomograms are clearly larger than those in the cryosections. In fact, the results of a *t*-test for the PM–PG and PG–OM distances in the tomograms and the cryosections were 5.0 and 0.4, respectively, which statistically supports the finding that the PM–PG distances obtained using the two methods were different, whereas the PG–OM distances were almost equal. Furthermore, even in the same tomogram, this latter distance differs in the lateral and pole positions, the space between PM and PG at the pole position being wider than at the lateral position. Visually, we can discern this difference by a snapshot of the bacterial cell.

## Discussion

As evidenced by the recent pioneering research on the cell envelopes of mycobacteria and corynebacteria by using CEMOVIS [16], the cryosectioning technique can successfully visualize the delicate OM structures, which would have been easily destroyed in conventional plastic sectioning, in members of the Corynebacterineae suborder. To facilitate comprehensive use of this technique, we tried to estimate the differences between whole-embedded cells and cryosectioned cells. To this end, we assumed that the tomograms of the whole-embedded cells reflect a closer-to-native structure than the tomograms of the cryosectioned cells and we tried to estimate the structural deformation caused by the cryosectioning process by measuring the distances between the layers in the cell envelope. Our results showed that the distances between PG and OM in tomograms and vitreous cryosections are similar to each other. On the other hand, the PM–PG distance is consistently smaller in cryosections, indicating that it is more susceptible to the mechanical stress caused by the cryosectioning. The pressure during the cutting process is produced mainly along the cutting direction. However, the perpendicular component to the cutting direction is also produced by a diagonal vector of the cutting pressure. This must push the specimen in the cross-direction. Thus, the cross-direction pressure shrinks the periplasmic space even at the edge region. Our results that shrinkage occurs in the periplasmic space by cryosectioning are in sharp contrast with the results reported by Hoffmann *et al.* [8]. Their data indicate that the centre-to-centre distance of the PM–OM space in tomograms and vitreous cryosections is 22 and 27.4 nm, respectively, which suggests that an approximate 25% dilation of the periplasmic space occurs as a result of vitreous cryosectioning. On the other hand, we obtained PM–OM distance values of 25.1 and 23 nm in tomograms and vitreous cryosections, respectively, corresponding to an 8% shrinkage. This was not caused by a difference in magnification. We acquired the images of cryosections and the tomography images by using the same microscope at the same magnification and accelerated voltage. One possible explanation for the different results obtained could be the difference in *E. coli* strain used; Hoffmann *et al.* used DH5α, whereas we used BL21. Alternatively, waving envelope layers might cause measurement errors. Another possibility is that the plane of the section may not be perpendicular to the membranes in CEMOVIS. If the plane of the section is oblique to the membrane, the distances in CEMOVIS tend to be larger than those in tomograms. We calibrated the pixel size of a CCD image at ×30 000 by using a catalase crystal before collecting data. However, we could not estimate the defocus values of the images by using the contrast transfer function because the first zeros were not clear. Therefore, the large defocus values may have changed the pixel size. Whatever the actual reason, these contrasting observations suggest the need of further studies using various other specimens, including crystals, to evaluate the effect of vitreous ice sectioning.

### Concluding remarks

Vitreous sectioning clearly makes cells or tissues appear more internally crowded than conventional sectioning. Although crevasses and compression, which are artefacts of vitreous sectioning, sometimes make it difficult to interpret the microstructures, vitreous specimen are essential for obtaining high molecular resolution. This is because non-chemically linked and non-deformed proteins are obtained in the vitreous phase, which are smaller in scale than crevasses, the size of which is usually a few dozen nanometres. The envelope layers of bacterial cells can be visualized in both whole-mounted specimens in vitreous ice and in vitreous sections. This is the main reason why we used *E. coli* to estimate the extent to which vitreous sectioning affects the architecture at the scale of a few dozen nanometres. In order to confirm that the observed shrinkage in vitreous sectioning is universal phenomenon, it is necessary to undertake more detailed assessments using different type of samples such as crystals.

## Acknowledgements

The authors wish to thank Takayuki Kato and Keiichi Namba of the Graduate School of Frontier Bioscience, Osaka University, for kindly providing the cryo-electron microscope facilities.

## Funding

CREST (proposal no. J075201012, JST, Japan to K-O.A. and K.I.); grants from the Targeted Proteins Research Program of the Ministry of Education, Culture, Sports, Science and Technology of Japan (proposal no. 07090030 to S.M. and 07070016 to K.I.).

## References

1 Zhang X, Settembre E, Xu C, Dormitzer P R, Bellamy R, Harrison S C, and Grigorieff N (2008) Near-atomic resolution using electron cryomicroscopy and single-particle reconstruction. *Proc. Natl. Acad. Sci. USA.* **105**: 1867–1872.

2 Al-Amoudi A, Chang J J, Leforestier A, Mcdowall A, Salamin L M, Norlen L P, Richter K, Blanc N S, Studer D, and Dubochet J (2004) Cryo-electron microscopy of vitreous sections. *EMBO J.* **23**: 3583–3588.

3 Al-Amoudi A, Studer D, and Dubochet J (2005) Cutting artefacts and cutting process in vitreous sections for cryo-electron microscopy. *J. Struct. Biol.* **150**: 109–121.

4 Richter K (1994) Cutting artefacts on ultrathin cryosections of biological bulk specimens. *Micron* **25**: 297–308.

5 Hsieh C E, Marko M, Frank J, and Mannella C A (2002) Electron tomographic analysis of frozen-hydrated tissue sections. *J. Struct. Biol.* **138**: 63–73.

6 Dubochet J, Mcdowall A W, Menge B, Schmid E N, and Lickfeld K G (1983) Electron microscopy of frozen-hydrated bacteria. *J. Bacteriol.* **155**: 381–390.

7 Matias V R, Al-Amoudi A, Dubochet J, and Beveridge T J (2003) Cryotransmission electron microscopy of frozen-hydrated sections of *Escherichia coli* and *Pseudomonas aeruginosa*. *J. Bacteriol.* **185**: 6112–6118.

8 Hoffmann C, Leis A, Niederweis M, Plitzko J M, and Engelhardt H (2008) Disclosure of the mycobacterial outer membrane: cryo-electron tomography and vitreous sections reveal the lipid bilayer structure. *Proc. Natl. Acad. Sci. USA* **105**: 3963–3967.

9 Iancu C V, Tivol W F, Schooler J B, Dias D P, Henderson G P, Murphy G E, Wright E R, Li Z, Yu Z, Briegel A, Gan L, He Y, and Jensen G J (2006) Electron cryotomography sample preparation using the Vitrobot. *Nat. Protoc.* **1**: 2813–2819.

10 Frederik P M and Hubert D H (2005) Cryoelectron microscopy of liposomes. *Meth. Enzymol.* **391**: 431–448.

11 Kremer J R, Mastronarde D N, and Mcintosh J R (1996) Computer visualization of three-dimensional image data using IMOD. *J. Struct. Biol.* **116**: 71–76.

12 Gilbert P (1972) Iterative methods for the three-dimensional reconstruction of an object from projections. *J. Theor. Biol.* **36**: 105–117.

13 Yasunaga T and Wakabayashi T (1996) Extensible and object-oriented system Eos supplies a new environment for image analysis of electron micrographs of macromolecules. *J. Struct. Biol.* **116**: 155–160.

14 Cavalier A, Spehner D, and Humbel B M (2009) *Handbook of Cryo-Preparation Methods for Electron Microscopy* (Boca Raton, CRC Press).

15 Iwasaki K, Mitsuoka K, Fujiyoshi Y, Fujisawa Y, Kikuchi M, Sekiguchi K, and Yamada T (2005) Electron tomography reveals diverse conformations of integrin alphaIIbbeta3 in the active state. *J. Struct. Biol.* **150**: 259–267.

16 Zuber B, Chami M, Houssin C, Dubochet J, Griffiths G, and Daffe M (2008) Direct visualization of the outer membrane of mycobacteria and corynebacteria in their native state. *J. Bacteriol.* **190**: 5672–5680.